

## Cross sections for elastic electron scattering by benzene at low and intermediate energies

Alexi de A. Cadena <sup>1</sup>, Alan G. Falkowski <sup>2</sup>, Ronald Pocaroba,<sup>1</sup> Regan Jones,<sup>1</sup> Mahak Mathur,<sup>3</sup> J. G. Childers <sup>1</sup>,  
Alessandra S. Barbosa <sup>4</sup>, Márcio H. F. Bettega <sup>4</sup>, Romarly F. da Costa <sup>5</sup>, Marco A. P. Lima <sup>2</sup>,  
Fábris Kossoski <sup>6,\*</sup> and Murtadha A. Khakoo <sup>1,†</sup>

<sup>1</sup>Department of Physics, California State University, Fullerton, California 92831, USA

<sup>2</sup>Instituto de Física “Gleb Wataghin”, Universidade Estadual de Campinas, Campinas, São Paulo 13083-970, Brazil

<sup>3</sup>Troy High School, 2200 Dorothy Lane, Fullerton, California 92831, USA

<sup>4</sup>Departamento de Física, Universidade Federal do Paraná, Caixa Postal 19044, Curitiba, Paraná 81531-980, Brazil

<sup>5</sup>Centro de Ciências Naturais e Humanas, Universidade Federal do ABC, Santo André, São Paulo 09210-580, Brazil

<sup>6</sup>Laboratoire de Chimie et Physique Quantiques (UMR 5626), Université de Toulouse, CNRS, UPS, 31062 Toulouse, France



(Received 15 November 2022; accepted 9 December 2022; published 26 December 2022)

We present experimental and theoretical differential cross sections for elastic electron scattering from benzene. The present experimental results are obtained at incident electron energies ranging from 1 to 50 eV and for scattering angles from 10° to 130°. The experimental measurements are compared to available results from 1 to 10 eV and to theoretical results from 10 to 50 eV, both based on the Schwinger multichannel (SMC) method. Different electron scattering calculations are carried out by employing varied basis sets and multichannel coupling schemes. This allows us to (i) obtain relatively converged cross sections with respect to the inclusion of Rydberg excited states, (ii) observe significant variations in the forward scattering as a function of the multichannel coupling scheme, and (iii) explore possible effects stemming from states lying above the ionization threshold. Overall, the agreement between experiments and models is found to be very good to excellent. The remaining discrepancies point out areas in which the SMC method should be improved.

DOI: [10.1103/PhysRevA.106.062825](https://doi.org/10.1103/PhysRevA.106.062825)

### I. INTRODUCTION

Electron scattering from polyatomic molecules at low incident electron energies has long been of great interest, for instance, in maintaining low-temperature plasmas used in the plasma processing industry, e.g., for chemical vapor deposition and plasma etching [1,2], where electron scattering cross sections are needed to model plasma environments [3,4]. In addition, low-energy electron scattering has been gaining further interest since the beginning of the new millennium, with the discovery that secondary electrons produced via ionizing radiation can cause single- and double-strand breaks in DNA [5,6]. This is understood to lead to mutations in living cells if the genetic code is not properly repaired [7]. Consequently, much work has been undertaken in both experimental and theoretical physics to provide cross-section data for low-energy electron scattering from polyatomic molecules, mostly for elastic scattering, which is usually the dominant channel and hence the natural first choice to model [8,9].

As a highly symmetrical molecule, benzene has much interest from a molecular structure point of view. From an experimental perspective, total electron scattering cross sections (TCSs) for this target were reported by Holst and Holtmark [10] for incident electron energies  $E_0$  up to 25 eV. Further TCSs were measured by Sueoka [11], Moze-

jko *et al.* [12], Makochehanwa *et al.* [13], and Kimura *et al.* [14]. These measurements reproduce structures around  $E_0 = 1.4$  eV and below 5 eV as reported by Nenner and Schultz [15] using electron transmission spectroscopy. Gulley *et al.* [16] measured very low  $E_0$  TCSs from nondeuterated benzene  $C_6H_6$  and deuterated benzenes  $C_6H_5D$  and  $C_6D_6$  at  $E_0$  from 35 meV to 2 eV. They observed that the  ${}^2E_{2u}$   $\pi^*$  shape resonance in  $C_6D_6$  was shifted up by approximately 25 meV from the same in  $C_6H_6$  (first vibrational level at 1.1 eV) with a Jahn-Teller distortion contribution in the resonant negative ion. They also observed a rapid increase in the TCS for  $E_0 < 100$  meV. More recently, Costa *et al.* [17] measured TCSs for benzene using a magnetically confined electron transmission beam system for  $E_0$  from 1 to 300 eV and a linear transmission electron beam apparatus for  $E_0$  from 100 to 1000 eV. The lower  $E_0$  TCSs were modeled using the Schwinger multichannel (SMC) method for  $E_0$  from 0.1 to 15 eV, whereas the independent-atom model with screening corrected additivity rule including interference effects was used to model TCSs for  $E_0$  from 10 to 1000 eV. They also observed a shape resonance at the  $E_0$  region of 1.4 eV and in the 4.6–4.9 eV region which they interpreted as a  $\pi^*$  shape resonance of  ${}^2B_{2g}$  symmetry. Costa *et al.* [17] also assigned a structure at 5.87 eV to a Feshbach resonance.

Differential elastic electron scattering cross sections (DCSs) were first reported by Gulley and Buckman [18] for benzene at  $E_0$  values of 8.5 and 20 eV and for scattering angles  $\theta$  up to 130°. Gussoni *et al.* [19] observed strong forward scattering due to the nonzero dipole polarizability of

\*fkossoski@irsamc.ups-tlse.fr

†mkhakoo@fullerton.edu

benzene ( $9.96 \text{ \AA}^3$ ) [20]. The first calculations were reported by Gianturco and Lucchese [21,22], who employed a potential scattering model to compute elastic DCSs, obtaining fair agreement up to 6 eV and overestimating the measurements of Gulley and Buckman at higher  $E_0$ . Shortly thereafter, Cho *et al.* [23] extended the measurements of Gulley and Buckman over a more extensive  $E_0$  range of 1.1–40 eV using the same apparatus as in Ref. [18]. They also monitored elastic scattering as a function of  $E_0$  at fixed  $\theta$  and found angular oscillatory structures (at  $\theta = 60^\circ, 90^\circ$ , and  $120^\circ$  for  $E_0$  from 0.95 to 1.65 eV) which moved significantly in  $\theta$  as a function of  $E_0$ . They also observed a strong resonance in their elastic scattering at  $E_0 = 5$  eV for their excitation function at  $\theta = 90^\circ$ . More recently, Jones *et al.* [24] experimentally observed the DCSs for elastic scattering of pyrimidine and benzene, at  $E_0 = 15$  and 30 eV, to be almost identical even for forward scattering. This was surprising since pyrimidine has a permanent dipole moment whereas benzene does not. However, pyrimidine has a polarizability (of only approximately 4% lower) similar to that of benzene [24]. Sanches *et al.* [25] measured elastic DCSs at intermediate to high  $E_0$  values of 50–1000 eV and  $\theta$  of up to  $130^\circ$  using an unselected electron gun. Similarly, Kato *et al.* [26] measured elastic DCSs for benzene at  $E_0$  values of 50, 100, and 200 eV, also as a precursor to normalizing their inelastic DCSs for differential excitation of the unresolved electronic states between 6 and 7 eV [27].

Along with the potential scattering calculation of Gianturco and Lucchese [21,22] there have been several other theoretical models developed. Initial *ab initio* work on electron scattering from benzene was made by Bettega *et al.* [28] using the SMC method within the static exchange and static exchange plus polarization levels of approximations. They reported elastic DCSs at nine  $E_0$  values ranging from 2.3 to 30 eV, which were compared with the experiment of Gulley and Buckman [18] with some but limited success. Field *et al.* [29] investigated the experimentally observed rapid rise of the TCS [16] below 0.2 eV and proposed the existence of a virtual state, further supported by later calculations with the SMC method [30]. Using a complex optical potential approach, de Souza *et al.* [31] calculated elastic scattering DCSs and TCSs for  $E_0$  from 20 to 500 eV. They compared their DCSs with those of the experiment of Cho *et al.* [23], Kato *et al.* [26], and de Souza *et al.* [31] and observed better agreement with experiments at higher  $E_0$  values. Bazante *et al.* [32] carried out an *ab initio* model of the  $E_{2u}$  shape resonance of benzene, finding its resonance energy  $E_0$  at approximately 1.6 eV. Most recently, Falkowski *et al.* [33] theoretically investigated elastic and electronically inelastic DCSs for benzene. They employed the SMC method to carry out scattering calculations, finding their elastic DCSs to be in good agreement with the measurement of Cho *et al.* from 15 to 30 eV, though discrepancies remain at lower and higher  $E_0$ . They also found satisfactory agreement with the DCSs of Kato *et al.* [27] for excitation of the bands in the 6–7 eV energy range.

In this work we revisit the elastic electron scattering DCSs from benzene over an extended  $E_0$  range of 1–50 eV to solidify the overall picture for this target and to resolve dif-

ferences between prior measurements. The data were divided into two ranges, viz., lower energies (1.0, 1.5, 2.0, 3.0, 5.0, and 8.5 eV) and intermediate energies (10.0, 12.5, 15.0, 20.0, 30.0, 40.0, and 50.0 eV), for  $\theta$  values of  $10^\circ$ – $130^\circ$ . The former were compared with calculations from Barbosa and Bettega [30] and the latter were compared to improved SMC calculations reported here. Our results are compared to the available experimental [23,25,26,31] and theoretical [22,30] DCSs.

The present study also raises a couple of practical questions concerning the applications with the SMC method. The projection operator  $P$ , which projects onto the space of open channels, plays a central role in the method. Several previous studies using the SMC method have shown that allowing progressively more channels in  $P$  tends to improve the comparison with experiment [34–41]. Typically, opening more channels causes the calculated elastic cross sections to decrease, thus approaching the experimental values from above, though with some overestimation. This effect is often referred to as convergence of the multichannel coupling. More recently, owing to improvements in the computational code and the description of target states [42], it has been possible to significantly increase the number of open channels in scattering calculations with the SMC method, reaching a record of 431 for ethanol [42] and 305 for benzene [33]. In these two recent applications [33,42] and also for formic acid [41], first indications of an interesting behavior showed up. In some cases, the computed elastic cross sections actually decreased “too much” when opening more channels, appearing below the experiment, inspiring important questions regarding the SMC method. What happens when we push the calculations by opening even more channels? If the cross sections are converging to numbers that are not close to the experiment, then what are the key limiting aspects of our current scattering models?

In this study we explore the convergence of the multichannel coupling while bearing in mind the above aspects, by posing two specific questions, concerning the truncation of Rydberg states and the impact of including states above the first ionization potential (IP). First, where should the infinite Rydberg series be truncated in order to obtain reasonably converged cross sections (with respect to the inclusion of additional Rydberg states)? Initial efforts to address this question were undertaken in a preliminary study [33], which is expanded here by consideration of additional and more elaborate scattering models. A major limitation of the SMC formalism concerns the ionization channels. Only bound states of the target are included in  $P$ , whereas the inclusion of ionized states is not allowed. On top of that, the scattering boundary condition associated with ionization is not accounted for within the SMC method. All in all, the method is not designed to work well above the first IP. Formally, the Lippmann-Schwinger equation does not have unique solutions for three-body systems, which makes things even more cumbersome [43]. In practice, the continuum of ionized states becomes discretized due to the expansion of the scattering wave function in finite-range square-integrable ( $L^2$ ) functions, thus limiting their description in applications with the SMC method. The impact of this approximation in the context of the SMC method is still

unclear, despite some modest success to model the elastic and electronic excitation cross sections above the IP. Here we ask whether there are any particular effects in closing exclusively the channels lying above the IP.

The remainder of the text is organized as follows. Section II outlines the details of the experimental measurements. The theory and computational details are presented in Sec. III. Our results are presented and discussed in Sec. IV, which are divided into three parts, about the elastic DCSs at lower  $E_0$  values from 1 to 10 eV (Sec. IV A) and intermediate  $E_0$  values from 10 to 50 eV (Sec. IV B), and the elastic integral cross sections (ICSs) and momentum transfer cross sections (MTCSS) (Sec. IV C). A summary is given and main conclusions are drawn in Sec. V.

## II. EXPERIMENTAL METHOD

The experimental setup at California State University Fullerton is detailed elsewhere [44]. Only a brief description is given here. The well-tested electron spectrometer, employing double hemispherical energy selectors, was made of titanium in both the electron gun and detector. Sets of 2.5-cm-diam cylindrical lenses were used to transport electrons through the spectrometer which was baked at about 80 °C–130 °C with magnetically free biaxial heaters [45] to keep the spectrometer surfaces stable. Electrons were detected by a discrete dynode electron multiplier [46] with a dark count rate of less than 0.01 Hz and could detect  $10^5$  electrons/s without saturating. The remnant magnetic field in the collision chamber was reduced to approximately 1 mG in the scattering center by the insertion of a double mu-metal shield. The standard electron current ranges from 18 to 30 nA, with an energy resolution of 40–70 meV full width at half maximum. Lower currents were chosen for lower  $E_0$  values to minimize space charge broadening of the incident electron beam. The electron beam could easily be focused at 1 eV and remained stable, with the current varying about 15% at maximum during a data acquisition period. The energy of the beam was established by measuring the minimum in the elastic scattering of the  $2^2S$  He<sup>-</sup> resonance at 19.366 eV [47] at a  $\theta$  of 90° to approximately 45 meV stability during a daily run. The contact potential varied between 0.65 and 0.85 eV. The elastic peaks of the energy loss spectra were collected at fixed  $E_0$  and  $\theta$  values by repetitive multichannel-scaling techniques. The effusive target gas beam was formed by flowing gas through an approximately 0.4-mm-diam thin aperture (approximately 0.025 mm thick), which was carbon sooted (using an acetylene flame, as were the spectrometer collision region surfaces) to reduce secondary electrons. The usage of an aperture source instead of a tube gas collimator removes the need to maintain the backing pressures of target gases in an inverse ratio of their molecular diameters (in order to equalize the mean free path of the two target gases [48] in the gas collimating structure), thus removing an additional systematic source of error that could occur in using a conventional tube collimator or similar setups (see, e.g., Ref. [48]). This is advantageous when working with heavy molecular targets with masses around 100 amu (such as benzene) as the uncertainty in the gas kinetic molecular diameters can be considerable and applying the inverse molecular diameter gas pressure ratio accurately in the relative flow

method (RFM) at moderate or high target source pressures is made more challenging with controlling the stability in the flow of these viscous mass targets through collimating needle sources. The aperture, located approximately 7 mm below the axis of the electron beam, was incorporated into a movable source [48,49] arrangement which moved the aperture into and out of alignment with the incident electron beam. The movable gas source method determined background electron-gas scattering rates expediently and accurately [49]. The measured DCSs were normalized using the RFM with helium as the reference gas. When applying the RFM, the pressures behind the aperture ranged from 1.3 to 1.9 Torr for He and from 0.13 to 0.15 Torr for benzene, resulting in target chamber pressure ranging from  $1.3 \times 10^{-6}$  to  $2.2 \times 10^{-6}$  Torr for benzene and from  $8 \times 10^{-7}$  to  $1.2 \times 10^{-6}$  Torr for He. The benzene liquid was obtained from Sigma-Aldrich with purity greater than or equal to 99.8%. The liquid was placed in a 50-cm<sup>3</sup> all glass-metal flask attached by baked 1/4-in. refrigeration copper tubing to the experimental gas handling system, which was also heated by the same biaxial heaters as above. The liquid sample was purified from dissolved gases by liquid-N<sub>2</sub> freeze-pump cycles. Benzene has a significant molecular mass (78.1 amu), increasing its viscosity which can cause periodic instabilities in the flow by partially choking up the gas metering valve (Granville-Phillips Series 203 valve [50]). To counter this, the valve and the entire gas line afterward were baked at a temperature of about approximately 80 °C–100 °C to prevent condensation of benzene in the valve and gas lines. Each DCS was taken a minimum of two times in a run to check its reproducibility, and a weighted average was made of multiple data runs to obtain the final DCSs. The relative flow normalization with helium used the DCSs of Nesbet [51] at  $E_0 \leq 20$  eV and those of Register *et al.* [52] at higher  $E_0$  values. We note here that benzene was found to be a reactive gas which causes the electron filament and spectrometer aperture to become contaminated within a few weeks, so the spectrometer was operated at lower chamber pressures to increase the duty cycle of the experiment. In this experiment, there was no need to separately normalize the benzene DCSs obtained to helium, as the profiles of the target gases were the same, i.e., cosine emission angle distributions, well known for an effusive thin aperture source. However, it was also possible to observe the stability of the experiment from separate full  $\theta$  runs of helium followed by benzene (or vice versa) at any fixed  $E_0$ . The DCSs for elastic scattering of electrons from benzene were obtained at  $E_0$  values of 1, 1.5, 2, 3.5, 8.5, 10, 15, 20, 30, 40, and 50 eV and  $\theta$  of 10°–130°.

The (conservative) uncertainties in the experimental results vary from about 11% to 13.5% and include uncertainties in the helium elastic DCSs of Nesbet [51] at  $E_0 \leq 20$  eV and those of Register *et al.* [52] (about 8% on average), uncertainties on flow rates for helium and benzene (3%–6%), statistical uncertainties of the scattered electron signal (about 5%–10%, which includes background subtractions that increase the signal uncertainties), and variance in the independent DCSs runs at a given  $E_0$  value (7%–11%). These uncertainties were added in quadrature.

The DCSs are extrapolated to  $\theta$  of 0° and 180° by visual extrapolation or employing supporting theoretical DCSs, similar to our work in acetylene [53]. The ICSs and MTCSS

are then determined from the DCSs weighted by  $\sin(\theta)$  and  $\sin(\theta)[1 - \cos(\theta)]$  integrating factors, respectively. These integrating factors bias the values of the ICSs and MTCSs to be less sensitive to extrapolations at small  $\theta$  and large  $\theta$  and typically add about 5%–8% to the DCSs overall errors.

### III. THEORY AND COMPUTATIONAL ASPECTS

The electron scattering calculations were performed with the SMC method [54–56] implemented with pseudopotentials [57]. The method has been reviewed elsewhere [58] and here we only provide the relevant details concerning this application. The working expression for the fixed-nuclei body-frame scattering amplitude is given by

$$f(\mathbf{k}_f, \mathbf{k}_i) = -\frac{1}{2\pi} \sum_{m,n} \langle S_{\mathbf{k}_f} | V | \chi_m \rangle (d^{-1})_{mn} \langle \chi_n | V | S_{\mathbf{k}_i} \rangle, \quad (1)$$

with

$$d_{mn} = \langle \chi_m | \left[ \frac{\hat{H}}{N+1} - \frac{\hat{H}P + P\hat{H}}{2} + \frac{VP + PV}{2} - VG_p^{(+)}V \right] | \chi_n \rangle. \quad (2)$$

The operator  $V$  is the interaction potential between the incident electron and the molecule,  $\mathbf{k}_i$  ( $\mathbf{k}_f$ ) is the incoming (outgoing) projectile wave vector, and  $\hat{H} = E - H$  is the total energy (target ground-state energy plus the kinetic energy of the incoming electron) minus the  $(N + 1)$ -electron Hamiltonian,  $N$  being the number of electrons in the target. The Hamiltonian is given by  $H = H_0 + V$ , where  $H_0$  describes the noninteracting electron-molecule system, and  $|S_{\mathbf{k}_i}\rangle$  is a solution of  $H_0$ , given by the product of a plane wave with momentum  $\mathbf{k}$  and a target state  $|\Phi_i\rangle$ . Here  $G_p^{(+)}$  is the Green's function projected onto the  $P = \sum_{\ell=1}^{N_{\text{open}}} |\Phi_\ell\rangle\langle\Phi_\ell|$  space, spanning  $N_{\text{open}}$  electronic target states. The  $|\chi_m\rangle$  are configuration state functions (CSFs) in terms of which the  $N + 1$  scattering wave function is expanded. The details of the present application concerning the CSFs  $|\chi_m\rangle$ , the target states  $|\Phi_i\rangle$ , and the projection operator  $P$  are provided later in this section.

In this study we present theoretical results for several different scattering models. We first outline the general picture and specific motivations behind these calculations, leaving the computational details for later. We employed three basis sets B1, B2, and B3, which include systematically more diffuse functions to describe higher-lying Rydberg states as accessible channels. For each basis set, we considered three multichannel coupling schemes, by progressively increasing the number of target states in the projection operator  $P$ . This gives rise to nine scattering models, which are schematically summarized in Table I. Two of them were presented in our previous study [33] and here we complete the chart by performing seven additional rounds of calculation. We designed three different multichannel coupling schemes based on the choice for the projection operator  $P$ : (i) only the elastic channel, (ii) all states below  $\epsilon_P = 9.09$  eV (the first IP according to Koopmans' theorem), and (iii) all states below  $\epsilon_P = 10$  eV. Note that the number of states in  $P$  also depends on the basis set, except of course for the elastic-only case.

There are three key justifications behind our several scattering calculations, which are in line with the questions raised

TABLE I. Summary of the nine scattering models discussed in this work.

Basis set	Projection operator $P$			No. of CSFs
	Elastic only	$\epsilon_P = 9.09$ eV	$\epsilon_P = 10$ eV	
B1	B1-1ch	B1-099ch	B1-117ch <sup>a</sup>	19775
B2	B2-1ch	B2-258ch	B2-305ch <sup>a</sup>	53281
B3	B3-1ch	B3-315ch	B3-437ch	86939

<sup>a</sup>Calculations originally reported in Ref. [33] and reproduced here.

at the end of Sec. I. First, it includes considerably more higher-lying Rydberg states as open channels by augmenting the basis set from B2 to B3 (bottom row in Table I), thus expanding upon our previous study [33] in this regard. This helps address the question concerning the truncation of the Rydberg series and how this affects the calculated cross sections. Second, by comparing the models associated with  $\epsilon_P = 9.09$  and 10 eV in Table I, we address whether there are any particular effects in closing exclusively the channels lying above the IP. Third, by performing the calculations indicated by “elastic only” in Table I, we investigate the limitations of a single-channel model, in a type of analysis similar to that performed in previous studies with the SMC method [34–40].

A summary of the steps to perform the scattering calculations is illustrated in Fig. 1, which guides the presentation in the remainder of this section. The ground-state geometry was obtained using the second-order Møller-Plesset perturbation theory and the aug-cc-pVDZ basis set. The electronic ground state was described at the Hartree-Fock (HF) level of theory, using Cartesian Gaussian functions (CGFs) for the valence electrons and pseudopotentials of Bachelet *et al.* [59] for the nuclei and core electrons. For both the geometry optimization and the ground-state description, the GAMESS package [60] was employed. Three basis sets were employed in this study, B1, B2, and B3, with the first two the same as presented in Ref. [33]. All share a common set comprising  $5s5p3d$  CGFs centered at the carbon atoms,  $4s/3s$  plus  $1p$  CGFs at the hydrogen atoms, and  $3s3p2d$  CGFs at the center of mass, whose exponents and coefficients were given before [33]. This set of CGFs defines the B1 basis set. The B2 basis set is generated by supplementing B1 with a  $3s3p$  set of diffuse functions at four extra centers (see Ref. [33] for details). Basis set B3 is built by adding a  $2s2p$  set (the first two  $s$  and first two

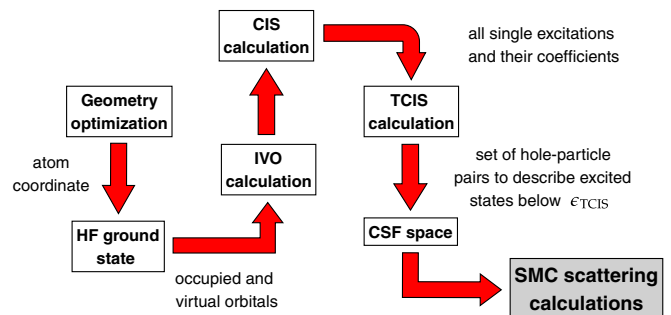


FIG. 1. Scheme illustrating the step-by-step procedure to perform SMC scattering calculations.

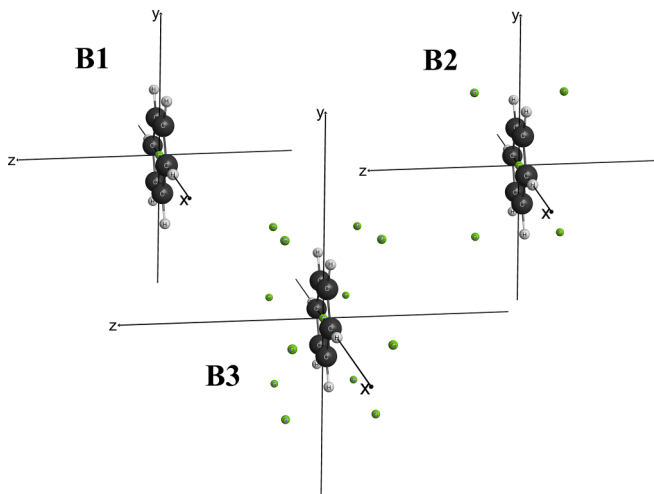


FIG. 2. Illustration of the extra centers (green spheres) in the B1 (one center), B2 (four centers), and B3 (13 centers) basis sets, generated with the wxMacMolPlt software [61].

$p$  functions of the  $3s3p2d$  set presented in Ref. [33]) in 12 extra centers. One extra center is placed at  $(6.7, 0.0, 3.0)a_0$ , assuming the molecule lies in the  $xy$  plane and that one C—H bond lies along the  $x$  axis, while the other centers are obtained according to the symmetries of the  $D_{6h}$  point group. The number, type, and position of the extra centers of basis set B3 were determined by maximizing the number of excited states below a given energy threshold, while making sure there are no linear dependence problems. Here we adopted 10 eV for this threshold, the same value that defines the multichannel coupling scheme, as explained later. Figure 2 shows the positions of the extra centers in the three basis sets. For basis set B3, this approach generated a scattering model at the limit of what is technically feasible with our current computational implementation.

From the HF calculation, we obtained the canonical molecular orbitals, occupied (hole) and virtual (particle). Since the virtual orbitals are not the most suitable to describe excited states, we employed instead improved virtual orbitals (IVOs) [62] by removing an electron from a specific hole and then diagonalizing the cationic Fock matrix in the virtual orbital space. Here we selected the uppermost occupied orbital and the triplet multiplicity, as in Ref. [33]. To obtain the electronically excited states, we employed the truncated configuration interaction with single excitations (TCIS) approach [42], which selects the most important single excitations for describing the states below a given energy  $\epsilon_{\text{TCIS}}$ , based on a preliminary calculation where all single excitations are included (CIS). The energy  $\epsilon_{\text{TCIS}}$  plays the role of an arbitrary threshold value that fixes the hole-particle pairs to include in the TCIS excited-state calculation. In general,  $\epsilon_{\text{TCIS}}$  is different from  $\epsilon_P$  (the maximum excitation energy of the target states to be included in the  $P$  projector). In previous studies on electron scattering from ethanol and benzene [33,42], the TCIS approach has been shown to account for a significant fraction of the states below  $\epsilon_{\text{TCIS}}$ , when compared with CIS. For the B1, B2, and B3 basis sets, the TCIS procedure gave rise to 117, 305, and 437 target states, respectively. It

is worth mentioning that all these states (for a given basis set) are considered to be open only in scattering calculations associated with  $\epsilon_P = 10$  eV (see Table I), while in the remaining calculations some of these states are imposed to be closed.

In the SMC method, the trial scattering wave function is written as a linear combination of CSFs, constructed by an antisymmetrized product of a target state and a scattering orbital. For each basis set, the CSF space for the static-exchange part is constructed from the HF ground state and the polarization CSFs are built using all the hole-particle pairs provided by the TCIS calculation as target states. In both cases, the full set of IVOs is employed as scattering orbitals, while keeping overall doublet CSFs. This procedure was followed for the three choices of the projection operator  $P$ , meaning that the same set of CSFs was employed for a given basis set (see Table I). Therefore, differences observed in the computed cross sections can be assigned to multichannel coupling effects. All calculations were performed in the  $D_{2h}$  point group. The details concerning the integration of the Green's function are the same as reported in Ref. [33].

## IV. RESULTS AND DISCUSSION

### A. Low energies (1–10 eV)

Our measured DCSs for impact energies from 1 eV up to 8.5 eV are presented in tabulated form in Table II (together with the ICS and MTCS) and are shown in Fig. 3. For the sake of comparison we also show in this figure the previous measurements by Cho *et al.* [23]. Also shown in Fig. 3 are the SMC results by Barbosa and Bettega [30] (labeled as SEP2 in Ref. [30]), which, along with the potential scattering model of Gianturco and Lucchese [22], considered only the elastic channel as being open. At  $\theta$  below approximately  $40^\circ$ , the present DCSs are significantly higher than those of Cho *et al.* [23] at  $E_0$  of 1 eV and somewhat higher at 2 and 3 eV. Notice that Cho actually reported DCSs at  $E_0$  of 1.1 eV, which are compared with our data at 1 eV. At  $E_0$  of 5 eV the DCSs of Cho *et al.* show a downward trend at small  $\theta$  not observed by the present experiment or the theory. The better agreement with theory suggests that the present measurements' DCSs are correctly above those of Cho *et al.* [23]. This systematic effect of lowered elastic scattering DCSs from the groups constituting Refs. [18,23] at small  $\theta$  and at low  $E_0$  had been observed by us at  $E_0$  of 2.0 eV in ethylene in [53] and we suggest that this could be due to background subtractions of scattered electrons at the small  $\theta$  in these experiments. This also suggests an advantage in using the movable gas source to determine backgrounds at small  $\theta$ . Otherwise, the agreement between the present experimental values and those of Cho *et al.* [23] is quantitatively excellent (in most cases within experimental uncertainties) for larger  $\theta$  values.

The experimental DCSs and the SMC results by Barbosa and Bettega [30] present an overall fair level of agreement above 4 eV. At the lowest  $E_0 \leq 4$  eV values, the theory does not quantitatively reproduce the dip in the experimental DCSs at  $\theta \approx 40^\circ$ , even though it resembles the measured form of the curves to some extent. In addition, the calculated DCSs appear underestimated at  $E_0$  of 2 and

TABLE II. Measured elastic electron scattering DCSs, ICSs, and MTCSs for benzene, with one standard deviation errors. Entries without errors (in italics) are obtained from extrapolation or interpolation. The DCSs are in units of  $10^{-16} \text{ cm}^2 \text{ sr}^{-1}$  and the ICSs and MTCSs are in units of  $10^{-16} \text{ cm}^2$ .

Angle (deg)	Energy											
	1 eV		1.5 eV		2 eV		3 eV		5 eV		8.5 eV	
0	8		8		8		<i>14</i>		22		55	
5	7		7		7		<i>12</i>		20		48	
10	<i>5.8</i>		<i>5.8</i>		<i>5.8</i>		9		<i>18</i>		<i>40</i>	
15	<i>4.6</i>		<i>4.6</i>		<i>4.6</i>		<i>7.3</i>		15.5		2.1	
20	3.66	0.51	3.79	0.49	3.78	0.50	5.79	0.76	12.1	1.6	22.3	2.90
25	2.75	0.34	2.84	0.38	3.13	0.39	4.84	0.60	9.68	1.19	14.4	1.91
30	2.45	0.30	2.23	0.29	2.76	0.34	3.82	0.47	7.91	0.96	10.9	1.42
40	2.27	0.28	1.70	0.22	3.10	0.45	3.88	0.56	6.91	0.99	5.89	0.77
50	2.11	0.25	2.01	0.26	3.00	0.37	4.27	0.52	5.27	0.63	3.36	0.44
60	2.17	0.26	2.40	0.31	3.27	0.40	4.18	0.51	3.60	0.44	1.93	0.25
70	2.24	0.27	2.50	0.33	3.12	0.39	3.47	0.43	2.59	0.32	1.86	0.24
80	2.15	0.26	2.41	0.31	2.40	0.29	2.45	0.30	1.78	0.21	2.01	0.26
90	2.14	0.26	2.19	0.28	2.41	0.30	1.50	0.18	1.68	0.20	1.87	0.24
100	1.71	0.21	1.90	0.25	1.70	0.21	1.35	0.17	1.70	0.21	1.82	0.24
110	1.44	0.18	1.87	0.24	1.41	0.17	1.09	0.13	1.71	0.21	2.02	0.26
120	1.25	0.16	1.42	0.18	1.13	0.14	1.23	0.15	1.72	0.21	1.80	0.23
125	<i>1.15</i>		<i>1.33</i>		<i>1.04</i>		<i>1.24</i>		<i>1.75</i>		<i>1.69</i>	
130	1.06	0.13	1.23	0.16	0.94	0.12	1.24	0.15	1.78	0.22	1.58	0.21
140	<i>0.85</i>		<i>0.85</i>		<i>0.75</i>		<i>1.2</i>		<i>2</i>		<i>1.45</i>	
150	<i>0.75</i>		<i>0.75</i>		<i>0.7</i>		<i>1.25</i>		<i>2.2</i>		<i>1.58</i>	
160	<i>0.85</i>		<i>0.85</i>		<i>0.85</i>		<i>1.24</i>		<i>2.4</i>		<i>1.7</i>	
170	<i>1.05</i>		<i>1.05</i>		<i>1.05</i>		<i>1.2</i>		<i>2.5</i>		<i>1.86</i>	
180	<i>1.3</i>		<i>1.3</i>		<i>1.3</i>		<i>1.3</i>		<i>2.55</i>		<i>2</i>	
ICS	23.3	3.3	24.5	3.5	27.0	3.9	31.6	4.5	42.6	6.1	47.5	6.8
MTCS	18.4	2.6	20.1	2.8	19.9	2.8	21.5	3.0	27.5	3.8	24.7	3.4

1.5 eV and most strikingly at  $E_0$  of 1 eV. A clear  $d$ -wave angular distribution at 1, 1.5, and 2 eV can also be seen in Fig. 3. At higher energies the  $d$ -wave character of the DCSs

is somewhat less evident, indicating an admixture of higher partial waves. The model potential results from Gianturco

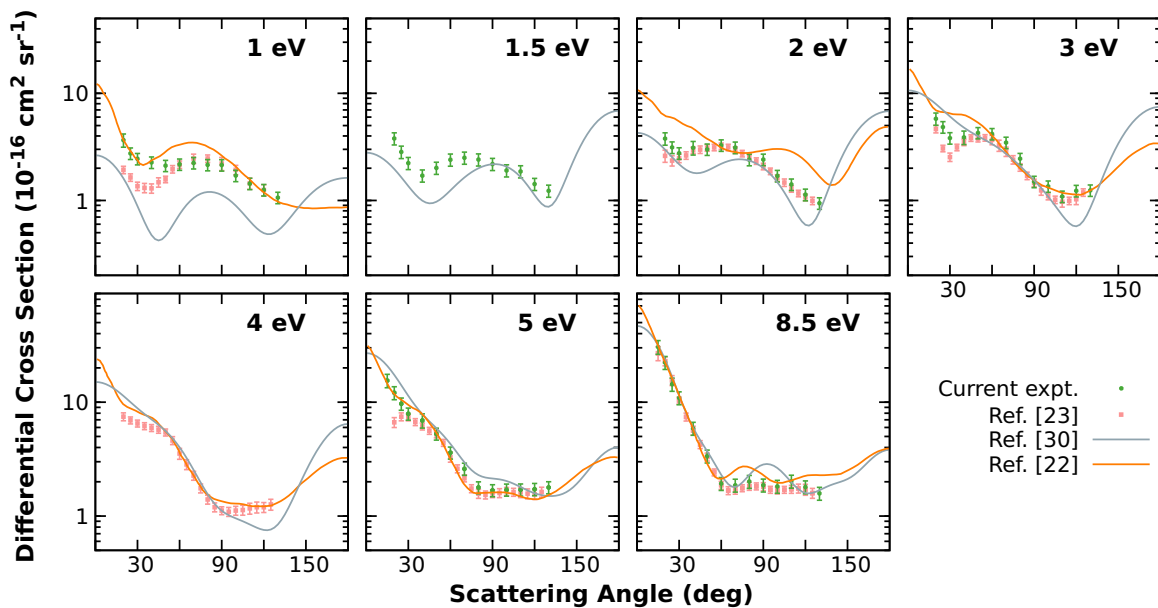


FIG. 3. Elastic differential cross sections for electron scattering from benzene, according to the current measurements and previous ones from Cho *et al.* [23], as well as calculations reported by Barbosa and Bettega [30] and by Gianturco and Lucchese [22].

TABLE III. Measured elastic electron scattering DCSs, ICSs, and MTCSs for benzene, with respective errors. Entries without errors (in italics) are obtained from extrapolation or interpolation. The DCSs are in units of  $10^{-16}$  cm<sup>2</sup> sr<sup>-1</sup> and the ICSs and MTCSs are in units of  $10^{-16}$  cm<sup>2</sup>.

Angle (deg)	Energy													
	10 eV		12.5 eV		15 eV		20 eV		30 eV		40 eV		50 eV	
0	<i>70</i>		<i>85</i>		<i>90</i>		<i>150</i>		<i>200</i>		<i>250</i>		<i>280</i>	
5	<i>60</i>		<i>70</i>		<i>73</i>		<i>120</i>		<i>120</i>		<i>140</i>		<i>150</i>	
10	<i>50</i>		<i>55</i>		<i>55</i>		<i>80</i>		61.6	9.0	66.1	9.1	44.1	6.5
15	39.8	5.5	44.4	6.1	36.9	5.1	43.6	6.0	25.1	3.5	20.1	2.7	18.5	2.6
20	31.0	4.0	29.2	3.9	19.7	2.6	19.9	2.6	10.8	1.4	6.53	0.79	4.90	0.67
25	18.9	2.5	19.0	2.3	12.3	1.5	10.7	1.3	4.46	0.53	2.65	0.32	2.19	0.28
30	12.1	1.6	9.60	1.16	6.68	0.80	4.47	0.53	1.81	0.21	1.53	0.18	1.45	0.18
40	5.20	0.68	3.49	0.42	2.05	0.24	1.05	0.12	0.80	0.10	1.25	0.16	1.01	0.12
50	2.94	0.38	1.73	0.22	1.01	0.13	0.648	0.077	0.890	0.106	0.959	0.118	0.661	0.086
60	1.83	0.24	1.31	0.16	1.04	0.13	0.845	0.103	0.649	0.079	0.549	0.065	0.335	0.043
70	1.95	0.25	1.59	0.19	1.16	0.14	0.941	0.109	0.514	0.060	0.387	0.046	0.259	0.032
80	2.33	0.30	1.86	0.22	1.31	0.16	0.892	0.104	0.415	0.049	0.342	0.040	0.235	0.029
90	2.27	0.30	1.86	0.22	1.26	0.15	0.694	0.080	0.385	0.045	0.391	0.046	0.238	0.029
100	2.32	0.30	1.87	0.22	1.13	0.13	0.618	0.072	0.412	0.049	0.406	0.048	0.246	0.030
110	2.30	0.30	1.67	0.20	1.01	0.12	0.852	0.100	0.486	0.055	0.465	0.055	0.276	0.034
120	1.86	0.24	1.70	0.20	1.06	0.12	0.894	0.104	0.558	0.067	0.636	0.082	0.302	0.037
125	<i>1.74</i>		<i>1.91</i>		<i>1.18</i>		<i>0.905</i>		0.606	0.082	0.722	0.091	0.363	
130	1.62	0.21	2.12	0.25	1.30	0.15	0.917	0.107	0.55		0.855	0.110	0.424	0.052
140	<i>1.5</i>		<i>2.3</i>		<i>1.5</i>		<i>1.1</i>		<i>0.8</i>		<i>0.85</i>		<i>0.55</i>	
150	<i>1.67</i>		<i>2.3</i>		<i>1.8</i>		<i>1</i>		<i>1</i>		<i>0.95</i>		<i>0.75</i>	
160	<i>1.8</i>		<i>2.3</i>		<i>2.1</i>		<i>1</i>		<i>1.5</i>		<i>1</i>		<i>0.85</i>	
170	<i>2</i>		<i>2.3</i>		<i>2.4</i>		<i>1</i>		<i>1.8</i>		<i>1</i>		<i>0.9</i>	
180	<i>2.2</i>		<i>2.4</i>		<i>2.7</i>		<i>1</i>		<i>2</i>		<i>1</i>		<i>0.95</i>	
ICS	54.5	7.8	50.9	7.3	38.3	5.5	37.8	5.4	26.5	3.8	26.4	3.8	21.9	3.1
MTCS	26.9	3.8	25.9	3.6	17.9	2.5	12.0	1.7	8.49	1.18	8.46	1.18	5.69	0.79

and Lucchese [22] show an overall better agreement with experiment, most notable at  $E_0$  of 1, 4, and 5 eV.

### B. Intermediate energies (10–50 eV)

We compare our measured DCSs for impact energies from 10 up to 50 eV, which are tabulated in Table III (together with the ICS and MTCS) and shown in Fig. 4 with previous measurements of Cho *et al.* [23], Sanches *et al.* [25], and Kato *et al.* [26]. In order to avoid possible threshold effects (as the last open channel appears at around 10.0 eV), the multichannel calculations were performed at  $E_0 = 10.5$  eV, just slightly above the energy in which the DCSs were measured ( $E_0 = 10.0$  eV). We find overall good agreement between the present data and the previous ones by Cho *et al.* [23], in shape and magnitude. At 50 eV excellent agreement is found between our measurements and the experimental data of Kato *et al.* [26], whereas those of Sanches *et al.* appear somewhat higher in magnitude.

We also show in Fig. 4 our theoretical results with the larger basis set (B3), for the three multichannel coupling schemes, together with the results of Barbosa and Bettega [30] at 10 eV. A detailed comparison with the results obtained with the B1 and B2 basis sets is performed later. Overall, our calculated DCSs are significantly closer to experiment than in previously reported calculations [22,25,28,30,31,63] and for this reason, here we do not reproduce and discuss all these previous results which can be encountered elsewhere [33].

Our theoretical results generally reproduce the experimental forward peak, even though important differences in shape and magnitude can still be observed at intermediate angles ( $\theta > 30^\circ$ ). The most notable ones appear for the B3-1ch model, which systematically overestimates the experimental data for all intermediate values of  $E_0$  and therefore entails a severe approximation in this energy range. The comparison to experiment significantly improves for the B3-315ch and B3-437ch schemes (shown in Fig. 4), clearly revealing important multichannel coupling effects. The elastic DCSs decrease in magnitude as the number of open channels in the projector  $P$  is augmented, since the inelastic channels now receive a share that would otherwise go to the elastic channel exclusively. In addition, by increasing  $E_0$ , we also found that such a drop in magnitude becomes less pronounced. This is because we only accounted for target states below 10 eV, which should have progressively less impact in the multichannel coupling as  $E_0$  increases. These findings have been observed in previous applications of the SMC method to other systems [33–35,39–42] and are confirmed again here.

Still considering  $\theta$  above approximately  $30^\circ$  and now looking at specific energies, we find at  $E_0 = 10$  and 12.5 eV that the B3-315ch model (only channels below the IP are open) shows very good agreement with experimental data, whereas the B3-437ch model underestimates them. At  $E_0 = 15$  and 20 eV, both models provide DCSs that are overall similar to each other and to the present and previous measurements. The

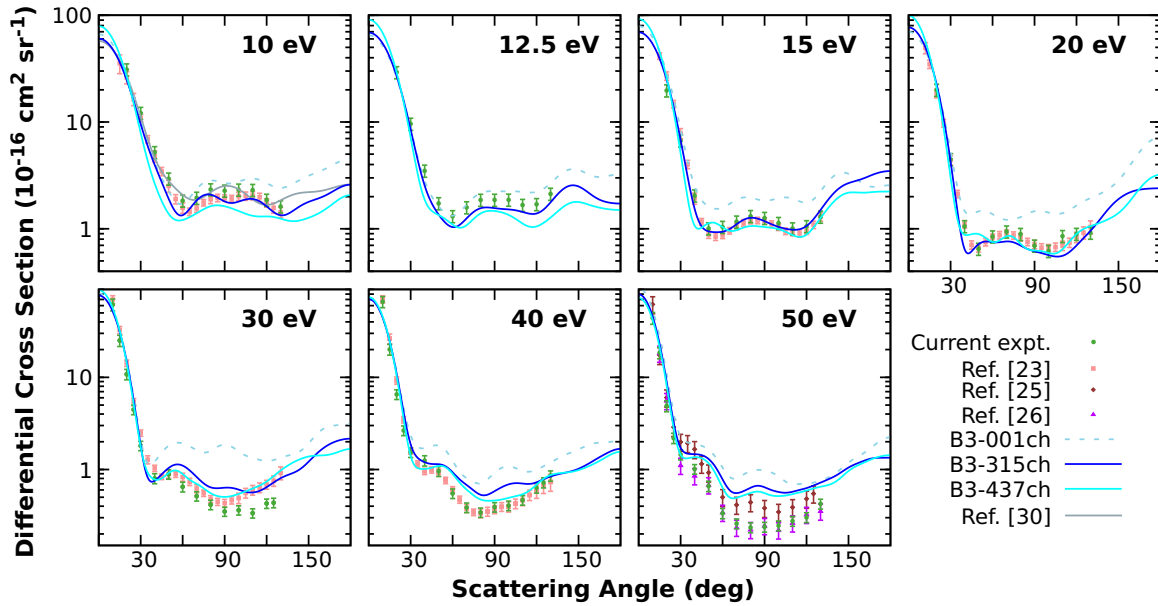


FIG. 4. Elastic differential cross sections for electron scattering from benzene, according to the current and previous measurements (from Cho *et al.* [23], Sanches *et al.* [25], and Kato *et al.* [26]), the present calculations with the B3 basis set and three multichannel coupling schemes, and the theoretical results of Barbosa and Bettega [30].

B3-315ch results generally overestimate both experimental data at  $E_0 = 30$  eV, whereas much better agreement with the present experiment can be seen with the B3-437ch model, the data from Cho *et al.* [23] appearing below. At  $E_0 = 40$  and 50 eV, even though all calculations overestimate the measured DCSs, the level of agreement improves when more open channels are accounted for. Such discrepancies are expected at these higher  $E_0$ , due to an increasing number of target states that become open and that are not included in our calculations. In particular, the ionization cross sections for benzene display a maximum in the 50–150 eV energy range [63–66]. Properly describing the scattering dynamics at this energy range would require accounting for a large number of not only discrete target states, but also the ionization channels, which should be paramount to improving the comparison to experiment. We further mention the SMC results of Barbosa and Bettega [30] for 10 eV. Their DCSs agree well with experiment, despite being a single-channel calculation, like our B3-1ch model. The two calculations adopt different approaches to include polarization effects, which may explain the difference between them.

Let us now discuss in detail our efforts to study the convergence of multichannel coupling using the nine scattering models described in Sec. III and listed in Table I. Figure 5 presents the full landscape of our theoretically obtained DCSs. The most important finding from this figure is that, for  $\theta$  above approximately  $30^\circ$ , the DCSs show convergence with respect to the inclusion of Rydberg states, which can be seen by comparing the solid lines in Fig. 5. By further augmenting the number of Rydberg states (going from B2-315ch to B3-437ch), the present results provide a firmer basis to the previous assertion [33] that higher-lying Rydberg states do not play an important role in the elastic channel, at least for  $\theta$  above approximately  $30^\circ$ . To study this regime, it is probably safe to truncate the infinite Rydberg series at relatively lower-

lying states (represented here by the B1 basis set) without seriously compromising the electron scattering calculations, as long as these states are taken as open in the calculations (as in B1-117ch). This is an important finding from a theoretical point of view (the results seem to converge despite the infinite number of states) and from a practical point of view (the B1-117ch model is much less computationally intensive than the B3-437ch model). We further notice that such basis-set effects become even milder as the impact energy increases (compare solid lines in Fig. 5), unless the target states are kept artificially closed, which then has a greater impact on the results (compare the dashed lines in Fig. 5). The observations discussed in the preceding paragraph for the B3 basis set also hold for the smaller B1 and B2 basis sets.

Notice that the previous discussion only covers  $\theta$  above approximately  $30^\circ$ . However, Fig. 5 shows that the different approximations of our scattering models also have a marked effect in the forward direction, at  $\theta$  less than approximately  $20^\circ$ . Compared to the higher values of  $\theta$ , such variations are less apparent from the logarithmic scale of the figure, but they are nonetheless quite significant and relevant, given the much larger DCSs at these small  $\theta$ . We can evaluate the impact of increasing the number of CGFs (left to right in columns 2–4 of Table I) and the level of multichannel coupling (top to bottom in Table I). For a given multichannel coupling scheme, augmenting the diffuseness of the CGFs extends the range of the potential seen by the incoming electron, explaining the rise of the DCSs in the forward direction (compare the solid lines at 10 eV in Fig. 5, which can be more easily appreciated). For single-channel calculations, the trend is more erratic, which underlines again the severe limitation of this approximation. More interestingly though, we can fix the basis set and appraise the effect of opening more channels at small  $\theta$ . We found that the largest DCSs at small  $\theta$  are observed for the models where all target states are considered open (e.g., B3-

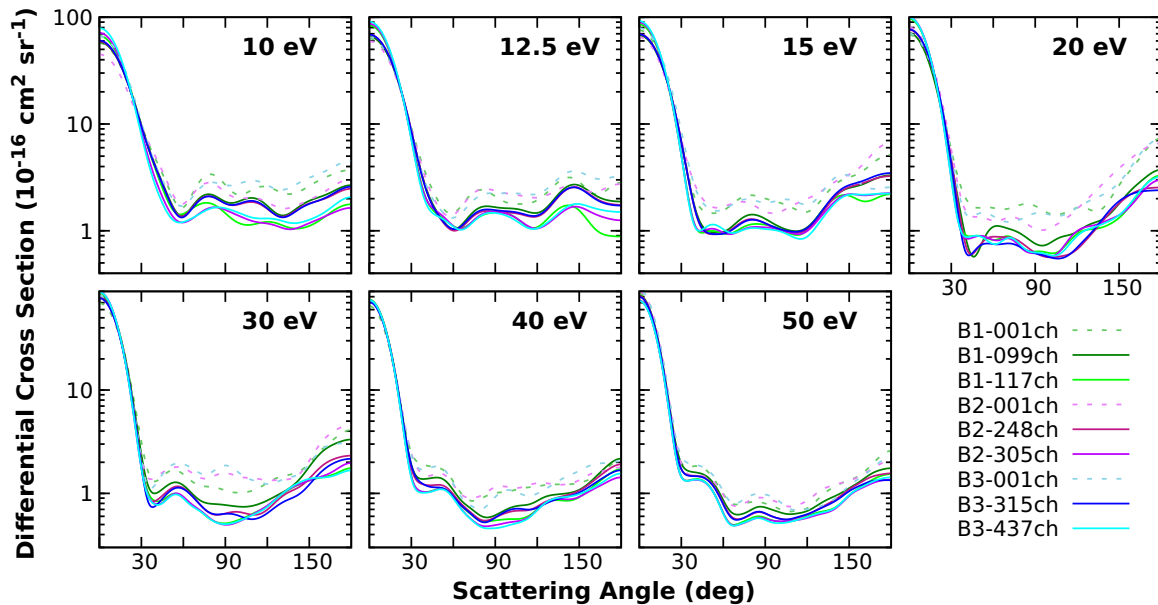


FIG. 5. Elastic differential cross sections for electron scattering from benzene, according to our nine scattering calculations. The B1-117ch and B2-315ch results were first reported in Ref. [33].

437ch), which is true for all basis sets and  $E_0$  (except for 50 eV). This is surprising at first because it seems to contradict the understanding that accounting for more channels tends to decrease the elastic DCSs due to these other competing channels. However, such larger forward-scattering elastic DCSs have a different origin. Enlarging the projection operator  $P$  effectively increases the range of the electron-target interaction potential  $V$  [see Eq. (2)], in close analogy to making the CGFs more diffuse, as discussed above.

We further assess any particular effects of including channels lying in the ionization continuum into the projection operator  $P$ . Opening these channels causes an overall decrease in the DCSs above  $\theta \approx 30^\circ$ , which is more pronounced at lower  $E_0$ , which would be expected for any other set of channels being opened. However, looking back at Fig. 4, we recall that at 10 and 12.5 eV, the B3-315ch model (where the states above the IP are closed) produces DCSs closer to experiment than the B3-437ch one (where such states are open). This specific comparison could suggest that the introduction of states above the IP would artificially lower the DCS to values below the experimental ones. This could be an unintended artifact from ignoring the continuum of ionized target states in the SMC method. In similar studies for ethanol [42] and formic acid [41], where channels lying above the IP were considered to be open, calculated elastic DCSs at higher energies also appeared to be underestimated with respect to experimental data. At this point, however, we cannot conclude that not properly describing the ionization is the ultimate cause of the small elastic DCSs.

### C. Elastic integral and momentum transfer cross sections

Figure 6 compares the elastic ICSs and MTCSs as obtained with the present and previous [23] measurements, as well as with the present calculations for intermediate  $E_0$

(above 10 eV) and previous calculations for lower  $E_0$  (below 10 eV) [30]. In the low-energy regime, the agreement between our calculated and measured results is generally good. The calculation correctly describes the decreasing ICSs towards lower  $E_0$ , even though the drop appears too steep with respect to the experimental data, with calculated ICSs slightly overestimated at  $E_0 = 5$  eV and then considerably underestimated at the lowest  $E_0$  of 1 eV. A similar contrast can be seen in the MTCSs for the same energy range. Some care is needed in these comparisons, however, as sometimes the calculations show significant increases in the backward direction (see Fig. 3), an experimentally inaccessible angular range. The calculated cross sections display two resonances. The lower-lying shape resonance belongs to the  $E_{2u}$  symmetry and the higher-lying resonance, which has mixed character of shape and core-excited resonance, belongs to the  $B_{2g}$  symmetry. Above approximately 5 eV, the ICS and MTCS present a series of pseudoresonances, which are associated with channels that are accessible at these energies but are kept closed to describe polarization effects.

At intermediate energies, the cross sections obtained with the B3-1ch calculation overestimate the experimental data (most notably the MTCSs). The calculated cross sections are considerably reduced in actual multichannel calculations (B3-315ch and B3-437ch) and generally lie within the experimental error bars, with some exceptions. At  $E_0 = 10$  and 12.5 eV, in particular, the agreement with the experimental data is better with the B3-315ch model, reflecting the previous discussion about the DCSs. Although not shown here, we observed similar trends with the B1 and B2 basis sets. This underlines again that we attained relatively converged cross sections with respect to Rydberg states. We also found minor basis-set effects in the ICS and MTCS, provided no channels were kept closed. The B3-315ch MTCSs overestimate the B3-437ch ones, with the difference decreasing progressively

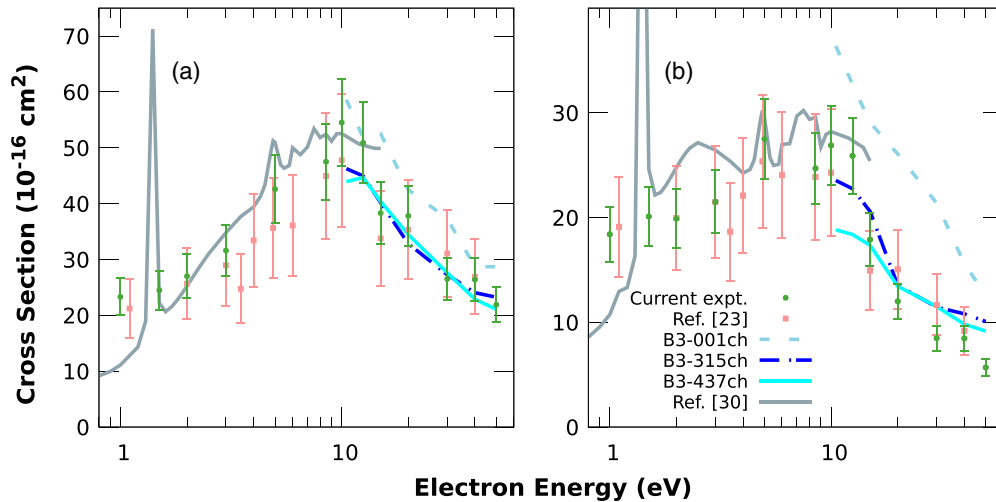


FIG. 6. (a) Elastic integral and (b) momentum transfer cross sections for electron scattering from benzene, according to the current measurements and previous ones from Cho *et al.* [23], together with the present calculations with the B3 basis set and three multichannel coupling schemes for the intermediate energies, and the theoretical results from Barbosa and Bettega [30] for the lower energies.

until 20 eV, where they follow more closely, reflecting the same behavior observed for the DCSs (Fig. 4 and Fig. 5). The above findings are therefore analogous to the ones regarding the DCSs.

The present measured elastic ICSs are compared with available experimental TCSs [11–13,16,17] in Fig. 7. The elastic channel clearly dominates at the lower energies, contributing progressively less towards higher energies, most noticeable above around 15 eV, where the ionization channels gain in importance. In the 1–2 eV range, the observed difference between the elastic ICSs and TCS indicates significant vibrational excitation mediated by the  $E_{2u}$  shape resonance.

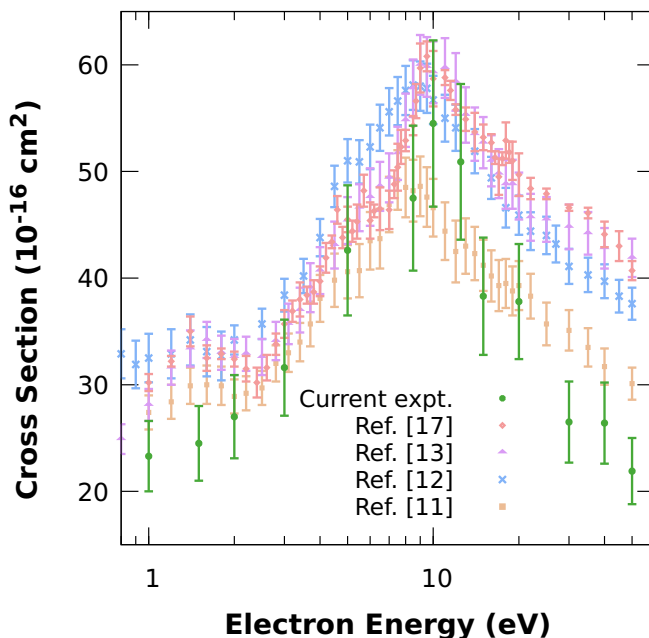


FIG. 7. Present measured elastic integral cross sections and available total cross sections as measured by Sueoka [11], Mozejko *et al.* [12], Makochekanwa *et al.* [13], and Costa *et al.* [17].

Previously calculated elastic ICSs [17,21,31,63,65,67–69] were compared in Ref. [30] (for the lower energies) and in Ref. [33] (for the intermediate energies) and therefore we do not repeat this discussion here.

## V. CONCLUSION

The present work presented a significantly improved picture of electron-benzene elastic scattering. We were able to provide elastic scattering experimental DCSs for benzene, covering a comprehensive energy range ( $E_0$  of 1–50 eV), which display overall very favorable agreement and some relatively minor disagreement with past empirical DCSs of Cho *et al.* [23], Sanches *et al.* [25], and Kato *et al.* [26]. Consequently, we reproduced DCSs for all the  $E_0$  values surveyed, which can be used to test scattering models like the present SMC calculations, targeted at  $E_0$  above 10 eV, as well as earlier single-channel SMC calculations for lower  $E_0$ . These calculations are in overall good agreement with experiments, despite some remaining discrepancies.

A central goal of this work was to study the convergence of the elastic DCSs with respect to the inclusion of progressively more Rydberg states in the calculations. For that, we explored nine different scattering models, by varying the diffuseness of the CGFs and the multichannel coupling scheme. The calculated DCSs at  $\theta$  above approximately  $30^\circ$  were found to be fairly converged in general, as long as the open channels were treated as such in the calculations. It remains to be seen how the multichannel coupling plays out with the inclusion of additional valence states (which would require augmenting the valence component of the CGFs). Moreover, we found that multichannel coupling effects affect not only how the flux is distributed between channels but likewise the elastic scattering in the forward direction. Finally, we observed somewhat better agreement with experiment at lower  $E_0$  when states lying above the first IP are artificially closed, which could derive from limitations of the SMC method regarding the ionization channels. Calculations that include such states should be explored carefully.

Some discrepancies with experiment still remain, with causes that depend on the specific energy. At the lowest energies ( $E_0 = 1 - 2$  eV), the calculated DCSs are systematically underestimated, which indicates deficiencies in the description of the quadrupolar potential and/or polarization of the target. At  $E_0 = 10$  and 12.5 eV, the calculations provide somewhat smaller DCSs than the experiment and the origin of this deviation is unclear. For higher energies ( $E_0 = 40$  and 50 eV), in contrast, the calculated DCSs are too large, suggesting that the inclusion of ionization effects in the SMC method should play an important role in improving the comparison with experimental data in this energy regime.

#### ACKNOWLEDGMENTS

A.G.F. acknowledges support from Coordenação de Aperfeiçoamento de Pessoal de Nível Superior, Brasil, Finance

Code 001, and M.A.P.L. and R.F.d.C. acknowledge the Brazilian agency Conselho Nacional de Desenvolvimento Científico e Tecnológico. This research used the computing resources and assistance of the John David Rogers Computing Center in the Institute of Physics “Gleb Wataghin”, University of Campinas. A.S.B. and M.H.F.B. acknowledge support from the Brazilian agencies Conselho Nacional de Desenvolvimento Científico e Tecnológico and computational support from Prof. C. M. de Carvalho at LFTC-DFis-UFPR and at LCPAD-UFPR. The work at California State University Fullerton (CSUF) was funded by the U.S. National Science Foundation, Research in an Undergraduate Institution, under Grants AMO No. 1606905 and No. 1911702. M.M. participated in the Troy Tech Summer Internship program. M.A.K. acknowledges the past invaluable help of CSUF technicians J. Woodland, A. Daveler, S. Bhari, and R. Wright for building and maintenance of the laboratory.

- 
- [1] W. N. G. Hitchon, *Plasma Processes for Semiconductor Fabrication* (Cambridge University Press, Cambridge, 1999).
- [2] M. A. Lieberman and A. J. Lichtenberg, *Principles of Plasma Discharges and Materials Processing* (Wiley, New York, 2005).
- [3] I. Adamovich, S. D. Baalrud, A. Bogaerts, P. J. Bruggeman, M. Cappelli, V. Colombo, U. Czarnetzki, U. Ebert, J. G. Eden, P. Favia, D. B. Graves *et al.*, *J. Phys. D* **50**, 323001 (2017).
- [4] L. Campbell and M. J. Brunger, *Plasma Sources Sci. Technol.* **22**, 013002 (2012).
- [5] B. Boudaiffa, P. Cloutier, D. Hunting, M. A. Huels, and L. Sanche, *Science* **287**, 1658 (2000).
- [6] Y. Zheng, J. R. Wagner, and L. Sanche, *Phys. Rev. Lett.* **96**, 208101 (2006).
- [7] E. V. Dyck, A. Z. Stasiak, A. Stasiak, and S. C. West, *Nature (London)* **398**, 728 (1999).
- [8] A. Garcia-Sanz, F. Carelli, F. Sebastianelli, F. A. Gianturco, and G. Garcia, *New J. Phys.* **15**, 013018 (2013).
- [9] M.-Y. Song, J.-S. Yoon, H. Cho, G. P. Karwasz, V. Kokoouline, Y. Nakamura, and J. Tennyson, *Eur. Phys. J. D* **74**, 60 (2020).
- [10] W. Holst and J. Holtsmark, *K. Nor. Vidensk. Selsk* **4**, 89 (1931).
- [11] O. Sueoka, *J. Phys. B* **21**, L631 (1988).
- [12] P. Moiejko, G. Kasperski, C. Szmytkowski, G. P. Karwasz, R. S. Brusa, and A. Zecca, *Chem. Phys. Lett.* **257**, 309 (1996).
- [13] C. Makochekanwa, O. Sueoka, and M. Kimura, *Phys. Rev. A* **68**, 032707 (2003).
- [14] M. Kimura, C. Makochekanwa, and O. Sueoka, *J. Phys. B* **37**, 1461 (2004).
- [15] I. Nenner and G. J. Schulz, *J. Chem. Phys.* **62**, 1747 (1975).
- [16] R. J. Gulley, S. L. Lunt, J. P. Ziesel, and D. Field, *J. Phys. B* **31**, 2735 (1998).
- [17] F. Costa, L. Álvarez, A. I. Lozano, F. Blanco, J. C. Oller, A. Muñoz, A. S. Barbosa, M. H. F. Bettega, F. Ferreira Da Silva, P. Limão-Vieira, R. D. White, M. J. Brunger, and G. García, *J. Chem. Phys.* **151**, 084310 (2019).
- [18] R. J. Gulley and S. J. Buckman, *J. Phys. B* **32**, L405 (1999).
- [19] M. Gussoni, M. Rui, and G. Zerbi, *J. Mol. Struct.* **447**, 163 (1998).
- [20] C. G. Le Févre and R. J. W. Le Févre, *J. Chem. Soc.*, 1577 (1954).
- [21] F. A. Gianturco and R. R. Lucchese, *J. Chem. Phys.* **108**, 6144 (1998).
- [22] F. A. Gianturco and R. R. Lucchese, *J. Chem. Phys.* **113**, 10044 (2000).
- [23] H. Cho, R. J. Gulley, K. Sunohara, M. Kitajima, L. J. Uhlmann, H. Tanaka, and S. J. Buckman, *J. Phys. B* **34**, 1019 (2001).
- [24] D. B. Jones, S. M. Bellm, P. Limão-Vieira, and M. J. Brunger, *Chem. Phys. Lett.* **535**, 30 (2012).
- [25] I. P. Sanches, R. T. Sugohara, L. Rosani, M. T. Lee, and I. Iga, *J. Phys. B* **41**, 185202 (2008).
- [26] H. Kato, M. C. Garcia, T. Asahina, M. Hoshino, C. Makochekanwa, H. Tanaka, F. Blanco, and G. Garcia, *Phys. Rev. A* **79**, 062703 (2009).
- [27] H. Kato, M. Hoshino, H. Tanaka, P. Limão-Vieira, O. Ingólfsson, L. Campbell, and M. J. Brunger, *J. Chem. Phys.* **134**, 134308 (2011).
- [28] M. H. F. Bettega, C. Winstead, and V. McKoy, *J. Chem. Phys.* **112**, 8806 (2000).
- [29] D. Field, J.-P. Ziesel, S. L. Lunt, R. Parthasarathy, L. Suess, S. B. Hill, F. B. Dunning, R. R. Lucchese, and F. A. Gianturco, *J. Phys. B* **34**, 4371 (2001).
- [30] A. S. Barbosa and M. H. F. Bettega, *J. Chem. Phys.* **146**, 154302 (2017).
- [31] G. L. C. de Souza, A. S. Dos Santos, R. R. Lucchese, L. E. Machado, L. M. Brescansin, H. V. Manini, I. Iga, and M.-T. Lee, *Chem. Phys.* **393**, 19 (2012).
- [32] A. P. Bazante, E. R. Davidson, and R. J. Bartlett, *J. Chem. Phys.* **142**, 204304 (2015).
- [33] A. G. Falkowski, R. F. da Costa, F. Kossoski, M. J. Brunger, and M. A. P. Lima, *Eur. Phys. J. D* **75**, 310 (2021).
- [34] R. F. da Costa, M. H. F. Bettega, M. A. P. Lima, M. C. A. Lopes, L. R. Hargreaves, G. Serna, and M. A. Khakoo, *Phys. Rev. A* **85**, 062706 (2012).
- [35] R. F. da Costa, M. H. F. Bettega, M. T. d. N. Varella, E. M. de Oliveira, and M. A. P. Lima, *Phys. Rev. A* **90**, 052707 (2014).
- [36] R. F. da Costa, E. M. de Oliveira, M. H. F. Bettega, M. T. d. N. Varella, D. B. Jones, M. J. Brunger, F. Blanco, R. Colmenares,

- P. Limão-Vieira, G. García, and M. A. P. Lima, *J. Chem. Phys.* **142**, 104304 (2015).
- [37] R. F. da Costa, M. T. d. N. Varella, M. H. F. Bettega, R. F. Neves, M. C. A. Lopes, F. Blanco, G. García, D. B. Jones, M. J. Brunger, and M. A. P. Lima, *J. Chem. Phys.* **144**, 124310 (2016).
- [38] D. B. Jones, F. Blanco, G. García, R. F. da Costa, F. Kossoski, M. T. d. N. Varella, M. H. F. Bettega, M. A. P. Lima, R. D. White, and M. J. Brunger, *J. Chem. Phys.* **147**, 244304 (2017).
- [39] R. F. da Costa, J. C. Ruivo, F. Kossoski, M. T. d. N. Varella, M. H. F. Bettega, D. B. Jones, M. J. Brunger, and M. A. P. Lima, *J. Chem. Phys.* **149**, 174308 (2018).
- [40] G. M. Moreira, F. Kossoski, M. H. F. Bettega, and R. F. da Costa, *J. Phys. B* **53**, 085002 (2020).
- [41] P. A. S. Randi, G. M. Moreira, and M. H. F. Bettega, *Eur. Phys. J. D* **75**, 306 (2021).
- [42] A. G. Falkowski, M. A. P. Lima, and F. Kossoski, *J. Chem. Phys.* **152**, 244302 (2020).
- [43] C. J. Joachain, *Quantum Collision Theory* (North-Holland, Amsterdam, 1975).
- [44] M. A. Khakoo, C. E. Beckmann, S. Trajmar, and G. Csanak, *J. Phys. B* **27**, 3159 (1994).
- [45] ARi Industries Inc., Addison, IL 60101, USA, 1HN040B-16.3 biaxial cable.
- [46] ETP Equipe Thermodynamique et Plasmas model AF151.
- [47] J. N. H. Brunt, G. C. King, and F. H. Read, *J. Phys. B* **10**, 433 (1977).
- [48] M. A. Khakoo, K. Keane, C. Campbell, N. Guzman, and K. Hazlett, *J. Phys. B* **40**, 3601 (2007).
- [49] M. Hughes, K. E. James, Jr., J. G. Childers, and M. A. Khakoo, *Meas. Sci. Technol.* **14**, 841 (2003).
- [50] MKS, Granville-Phillips Division, 6450 Dry Creek Parkway, Longmont, CO 80503, USA.
- [51] R. K. Nesbet, *Phys. Rev. A* **20**, 58 (1979).
- [52] D. F. Register, S. Trajmar, and S. K. Srivastava, *Phys. Rev. A* **21**, 1134 (1980).
- [53] A. Gauf, C. Navarro, G. Balch, L. R. Hargreaves, M. A. Khakoo, C. Winstead, and V. McKoy, *Phys. Rev. A* **87**, 012710 (2013).
- [54] K. Takatsuka and V. McKoy, *Phys. Rev. A* **24**, 2473 (1981).
- [55] K. Takatsuka and V. McKoy, *Phys. Rev. A* **30**, 1734 (1984).
- [56] M. A. P. Lima, L. M. Brescansin, A. J. R. da Silva, C. Winstead, and V. McKoy, *Phys. Rev. A* **41**, 327 (1990).
- [57] M. H. F. Bettega, L. G. Ferreira, and M. A. P. Lima, *Phys. Rev. A* **47**, 1111 (1993).
- [58] R. F. da Costa, M. T. d. N. Varella, M. H. F. Bettega, and M. A. P. Lima, *Eur. Phys. J. D* **69**, 159 (2015).
- [59] G. B. Bachelet, D. R. Hamann, and M. Schlüter, *Phys. Rev. B* **26**, 4199 (1982).
- [60] G. M. J. Barca, C. Bertoni, L. Carrington, D. Datta, N. De Silva, J. E. Deustua, D. G. Fedorov, J. R. Gour, A. O. Gunina, E. Guidez, T. Harville *et al.*, *J. Chem. Phys.* **152**, 154102 (2020).
- [61] B. M. Bode and M. S. Gordon, *J. Mol. Graph. Model.* **16**, 133 (1998).
- [62] W. J. Hunt and W. A. Goddard III, *Chem. Phys. Lett.* **3**, 414 (1969).
- [63] D. Prajapati, H. Yadav, P. Vinodkumar, C. Limbachiya, A. Dora, and M. Vinodkumar, *Eur. Phys. J. D* **72**, 210 (2018).
- [64] J. N. Bull, J. W. L. Lee, and C. Vallance, *Phys. Chem. Chem. Phys.* **16**, 10743 (2014).
- [65] S. Singh, R. Nagma, J. Kaur, and B. Antony, *J. Chem. Phys.* **145**, 034309 (2016).
- [66] W. Zhou, L. Wilkinson, J. W. L. Lee, D. Heathcote, and C. Vallance, *Mol. Phys.* **117**, 3066 (2019).
- [67] Y. Jiang, J. Sun, and L. Wan, *Phys. Rev. A* **62**, 062712 (2000).
- [68] J. Sun, C. Du, and Y. Liu, *Phys. Lett. A* **314**, 150 (2003).
- [69] S. Tonzani, *Comput. Phys. Commun.* **176**, 146 (2007).